Acta Crystallographica Section A
Foundations of Crystallography
ISSN 0108-7673

Received 29 November 2002
Accepted 14 April 2003

Secondary extinction and diffraction behaviors in cylindrical crystals[1]

Hua-Chen Hu

China Institute of Atomic Energy, PO Box 275 (18), Beijing 102413, People's Republic of China. Correspondence e-mail: hchu@ht.rol.cn.net

The X-ray and neutron diffraction properties in absorbing cylindrical crystals are systematically explored within the framework of transfer equations and the kinematic diffraction approximation. The calculated power ratio distribution, the integrated reflection power ratio and the secondary-extinction factor y_μ are expressed as functions of the Bragg angle θ_B, the reduced radius $\sigma_0\rho = \tau_0$ and the ratio of absorption coefficient to diffraction cross section $\mu/\sigma_0 = \xi_0$. Numerical solutions were obtained for all θ_B (0–90°) and samples with τ_0 from 0 to 30, and ξ_0 from 0 to 25. The relationship between the power ratio distribution curves, the integrated reflection power ratio and the diffraction geometry of cylindrical crystals is obtained for the first time and analyzed in detail. A dip was found in the curve of the extinction factor y_μ against τ_0 for given θ_B and ξ_0, and the position of this minimum shifts toward smaller τ_0 with increasing ξ_0 or θ_B. A large decrease of y_μ with decreasing θ_B at low angle appears when $\mu\rho > 3.5$ and $25 > \xi_0 > 0.2$. The rate of change of y_μ in this region increases with τ_0. All of this will be important for the refinement of diffraction data. The influence of different kinds of mosaic distributions on the integrated reflection power ratio and the extinction factor was also studied. The transmission coefficients A^* were calculated using two different methods, and an inaccuracy of these numbers in Vol. II of *International Tables for X-ray Crystallography* (1972) in the range $\theta_B \leq 15°$ and $\mu\rho \geq 15$ was found by comparison.

1. Introduction

Hamilton (1957, 1963) first studied the dependence of extinction on crystal shape and presented a table of secondary-extinction factors for cylindrical crystals without absorption. Becker & Coppens (1974*a*,*b*) significantly improved Zachariasen's (1967) theory of extinction for spherical crystals in X-ray diffraction. Their methods have been widely used in structure-factor refinement. In addition, there are many other works related to primary and secondary extinction in single crystals such as Werner (1974), Becker (1975, 1977), Kato (1976*a*,*b*, 1980*a*,*b*,*c*), Olekhnovich & Olekhnovich (1980), Wilkins (1981), Kawamura & Kato (1983), Becker & Dunstetter (1984), Sabine (1988), Al Haddad & Becker (1990), Chukhovskii *et al.* (1998), Thorkildsen & Larsen (1998*a*). However, the physical description and behavior of extinction for absorbing cylindrical and spherical crystals is inadequate, particularly for large extinction. Whether the primary extinction or secondary extinction is dominant in the case of low θ_B still remains obscure.

Wilkins (1981), Thorkildsen & Larsen (1999) and Authier (2001) studied the X-ray diffraction intensity pattern from finite perfect and imperfect crystals by the dynamical diffraction theory, but until now there has been no report on the investigation of the diffracted intensity profile from cylindrical mosaic crystals.

A systematic study of the transfer equations has been carried out by the author. Hu & Fang (1993) for the first time deduced the one-dimensional power transfer equations and gave exact solutions for plane-parallel and bent mosaic crystal plates in asymmetric Bragg and Laue geometry for the non-absorbing case. The reflectivity or reflection power ratio and integrated reflection power ratio for absorbing bent crystals were evaluated based on the layer coupling model (Hu, 1992; Hu & Fang, 1993). The diffraction behavior and secondary extinction for a plane-parallel mosaic crystal plate were derived for the first time through the exact solutions of the power transfer equations by the author (Hu, 1997*a*,*b*; see also Sears, 1997), and a preliminary study of the extinction of cylindrical and spherical crystals was also carried out (Hu, 1997*b*; Hu *et al.*, 2001). All the results calculated by these methods for crystal plates are in excellent agreement with experimental results.

This paper is a unified treatment without any approximation of the secondary-extinction factor y_μ for cylindrical crystals having rectangular, Gaussian or Lorentzian mosaic distributions within the framework of the transfer equations. It also includes an investigation of the relationship between diffrac-

[1] Project supported by National Nature Science Foundation of China and Science Foundation of Nuclear Industry of China.

tion geometry and power ratio profile, of the integrated reflection power ratio, as well as of y_μ for cylindrical crystals. The numerical solutions of the transfer equations based on the Euler integration method developed by Hamilton (1963) will be used.

Notation: In the following, RPR and $\mathrm{RPR}^{\mathrm{av}}$ designate the reflection power ratio and its average over the diameter of the cylinder as calculated from the transfer equations, and RPR_k represents the reflection power ratio from the kinematic approximation. An analoguous notation is adopted for the integrated reflection power ratio (IRPR).

2. Method

Hamilton (1963) first used the power transfer equations for the calculation of IRPR and the secondary-extinction factor for cylindrical crystals by substituting power for intensity in the Darwin transfer equations (Darwin, 1922). This makes the RPR for a cylindrical crystal identical with the intensity ratio I_H/I_0, and different from the case of an infinite plane-parallel crystal with asymmetric geometry (Hu, 1997*a*).

If the power in the incident beam with direction **N** is denoted by P_0 and the one in the diffracted beam with direction **M** by P_H, the transfer equations are

$$\frac{\partial P_H}{\partial m} = -(\mu+\sigma)P_H + \sigma P_0 \quad (1a)$$

$$\frac{\partial P_0}{\partial n} = -(\mu+\sigma)P_0 + \sigma P_H \quad (1b)$$

and for the kinematic approximation

$$\frac{\partial P_H}{\partial m} = -\mu P_H + \sigma P_0 \quad (2a)$$

$$\frac{\partial P_0}{\partial n} = -\mu P_0, \quad (2b)$$

where μ is the linear absorption coefficient or absorption cross section per unit volume for X-rays. For neutrons, μ is the attenuation coefficient, which is composed of nuclear absorption, and bound coherent and incoherent scattering cross sections per unit volume (Sears, 1989). σ is used instead of Σ_s (Hu, 1997*a*,*b*) for the diffraction cross section per unit volume (Becker & Coppens, 1974*a*) or coherent elastic scattering cross section per unit volume in a mosaic crystal (Hu, 1997*a*),

$$\sigma = QW(\Delta\theta_0), \quad (3)$$

where $W(\Delta\theta_0)$ is the distribution function of mosaic blocks, $\Delta\theta_0$ denotes the angular deviation of a reflecting plane from the average orientation. Q is the average scattering cross section per unit volume (Becker & Coppens, 1974*a*).

Three kinds of mosaic distribution functions are considered:

(i) rectangular distribution

$$W(\Delta\theta_0) = \begin{cases} 1/(2\eta\times 3^{1/2}) & \text{if } |\Delta\theta_0| \le \eta\times 3^{1/2} \\ 0 & \text{if } |\Delta\theta_0| > \eta\times 3^{1/2}; \end{cases} \quad (4)$$

(ii) Gaussian distribution

$$W(\Delta\theta_0) = [1/\eta(2\pi)^{1/2}]\exp\{-[\Delta\theta_0]^2/2\eta^2\}; \quad (5)$$

(iii) Lorentzian distribution

$$W(\Delta\theta_0) = [1/\eta(2\pi)^{1/2}][1+\pi(\Delta\theta_0/\eta)^2/2]^{-1}. \quad (6)$$

The reduced radius $\sigma\rho$ is defined as $\tau = \sigma\rho$. The values of τ and ξ at $\Delta\theta_0 = 0$ are defined as τ_0 and ξ_0.

$$\tau_0 = \sigma_0\rho \quad (7)$$

$$\xi_0 = \mu/\sigma_0. \quad (8)$$

The calculations were carried out in the oblique coordinate with twice the Bragg angle $2\theta_B$ between the two axes **M** and **N**, as shown in Fig. 1. Assume that the circular cross section of the cylindrical crystal is inscribed in a rhombus with the length of all four sides equal to $2\rho/\sin 2\theta_B$. The numerical calculation aims to solve the system of equations (1*a*), (1*b*), (2*a*) and (2*b*) over a regular mesh of grid points within the circle. The mesh was generated in such a way that the grid point spacing, $\Delta m = \Delta n$, is equal to $2\rho/n_0$ along the oblique coordinates, and the total number of grid points is $n_{\max} = n_0/\sin 2\theta_B$, $n_{\max} = m_{\max}$. In the present work, $n_0 \ge 200$. The incident radiation travels along the **N** direction and over each increment of Δm a power of P_0^0 is assumed to strike at a grid point on the boundary of the cylinder. The details of the formulae of a circle in the oblique coordinate system are deduced in Appendix *A*. The program was written in Fortran.

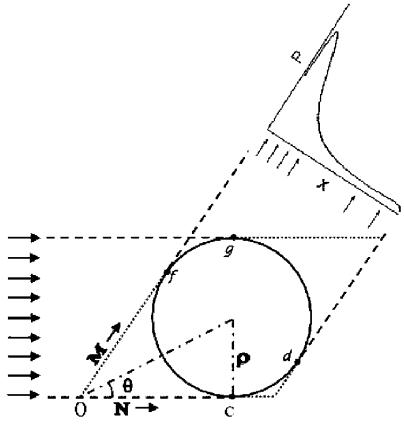

Figure 1
Schematic diagram of the diffraction geometry for a cylindrical crystal.

2.1. Integrated reflection power ratio

The integrated reflection power ratio[2] R_H^θ (IRPR) derived from the transfer equations (1*a*) and (1*b*) for a cylindrical crystal with height h and a rectangular mosaic distribution is

$$R_H^\theta(\xi_0,\tau_0)/\eta = 2\times 3^{1/2}h\Delta n\sin 2\theta_B P_H^{\mathrm{Total}}(\xi_0,\tau_0)/P_0^0, \quad (9)$$

where

[2] The left-hand side of (27) in Hu (1997*b*) should read $R_H^\theta/\eta(\xi_0,\Sigma_{s0}\rho)\,\mathrm{d}z$.

$$\sigma_0 = Q/2 \times 3^{1/2}\eta \tag{10}$$

$$P_H^{\rm Total}(\xi_0, \tau_0) = \sum_{n=1}^{n_{\max}} P_H[\xi_0, \tau_0, m_{\max}(n)]. \tag{11}$$

R_H^θ for a cylindrical crystal with Gaussian or Lorentzian mosaic distribution is

$$R_H^\theta(\xi_0, \tau_0)/\eta = h\Delta n \sin 2\theta_B \times \int_{-\infty}^{+\infty} \sum_{n=1}^{n_{\max}} P_H[\xi(\Delta\theta_0/\eta), \tau(\Delta\theta_0/\eta), m_{\max}(n)]\, {\rm d}(\Delta\theta_0/\eta)/P_0^0, \tag{12}$$

where

$$\sigma_0 = Q/(2\pi)^{1/2}\eta \tag{13}$$

for both distributions. σ depends also on the type of mosaic distribution and on $\Delta\theta_0/\eta$ in accordance with (3), (5) and (6), and $\xi(\Delta\theta_0/\eta) = \mu/\sigma(\Delta\theta_0/\eta)$.

$P_H^{\rm Total}$ in equations (9) and (12) is obtained through (11) by substituting the coefficients $C11$, $C12$, $C21$, $C22$ derived from (H8)[3] into (H7). The kinematic approximation of IRPR$_k$ for a cylindrical crystal with volume V is

$$R_k^\theta(\xi_0, \tau_0) = QA(\mu\rho)V = QA(\xi_0, \tau_0)V, \tag{14}$$

where $A(\mu\rho)$ is the transmission coefficient, and $\mu\rho = \xi_0\tau_0$, $V = \pi\rho^2 h$. R_k^θ can also be derived from (2a), (2b), (10) and (13) by the following expressions:

$$R_k^\theta(\xi_0, \tau_0)/\eta = 2 \times 3^{1/2}\sigma_0 A(\xi_0, \tau_0)V \tag{15}$$

for the rectangular mosaic distribution and

$$R_k^\theta(\xi_0, \tau_0)/\eta = (2\pi)^{1/2}\sigma_0 A(\xi_0, \tau_0)V \tag{16}$$

for the Gaussian and the Lorentzian mosaic distributions, where

$$\sigma_0 A(\xi_0, \tau_0)V = h\Delta n \sin 2\theta_B P_H^{\rm Total}(\xi_0, \tau_0)/P_0^0. \tag{17}$$

$P_H^{\rm Total}$ in (17) is obtained through (11) by substituting the coefficients $C11$, $C12$, $C21$, $C22$ derived from (H9) into (H7). From the above, one can also see that $A(\mu\rho) = R_k^\theta(\xi_0, \tau_0)/QV$.

2.2. Secondary-extinction factor

The secondary-extinction factor is defined as

$$y_\mu(\xi_0, \tau_0) = R_H^\theta(\xi_0, \tau_0)/QAV. \tag{18}$$

In order to improve the accuracy of the calculation, y_μ for the rectangular mosaic distribution is obtained by division of (9) by (15). Similarly, y_μ for the Gaussian and Lorentzian mosaic distributions is obtained by dividing (12) by (16). These expressions are exact for neutron diffraction. In the case of polarized X-rays, according to Becker & Coppens (1974a), $Q\cos^2 2\theta_B$ and $Q \times 1$ should be used instead of Q for obtaining the parallel and perpendicular components $y_{\mu||}(\xi_{0||}, \tau_{0||})$ and $y_{\mu\perp}(\xi_{0\perp}, \tau_{0\perp})$, respectively. For unpolarized X-rays,

$$y_\mu = (y_{\mu\perp} + y_{\mu||}\cos^2 2\theta_B)/2. \tag{19}$$

In the reanalysis of the diffraction data of LiF and MgO (Lawrence, 1972, 1973), $Q(1 + \cos^2 2\theta_B)/2$ was used to evaluate y_μ (Hu, 1997b). For a large sample, this may lead to deviations from y_μ defined by (19). For example, y_μ obtained by this alternative method may be 10% larger than the value from (19) when $\theta_B = 15^\circ$, $\tau_0 = 10$, $\xi_0 = 1.18$ and $\cos^2 2\theta_B = 0.75$. Therefore, matching y_μ from (19) to $y_{\rm obs}$ by varying σ_0 for given μ, ρ and Q gives a smaller value for σ_0 and corre-

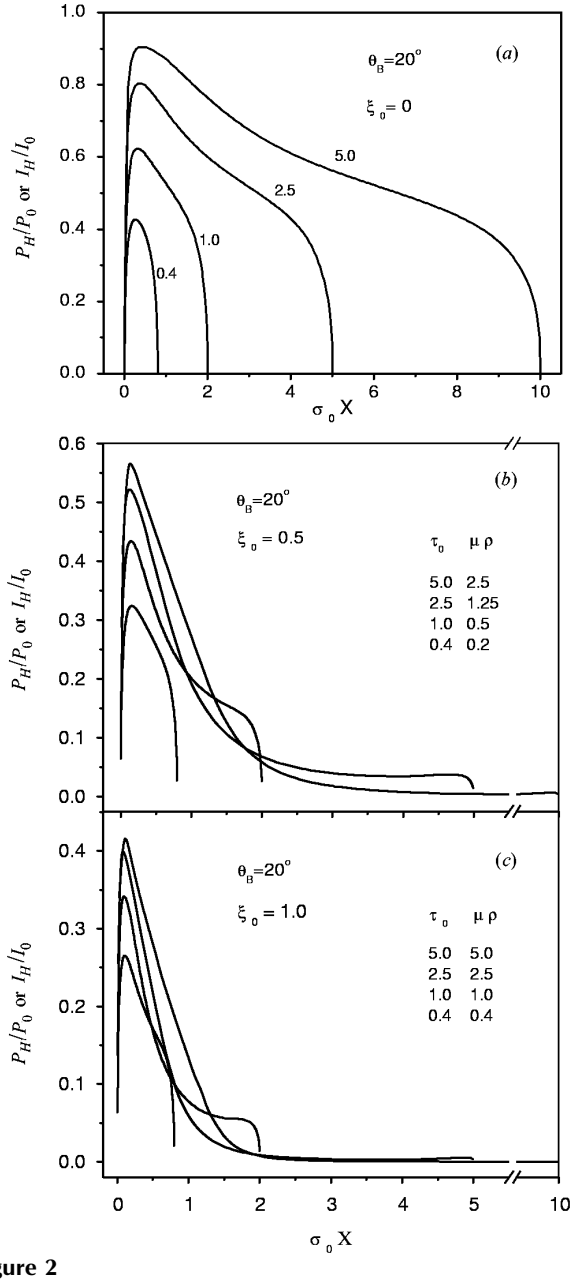

Figure 2
Power ratio distribution for cylindrical crystals with rectangular mosaic distribution and different values of ξ_0, τ_0 and $\mu\rho$. In (a), $\mu = 0$, and the curves are labeled with τ_0.

[3] Equation (8) in Hamilton's (1963) paper is here referred to by (H8). $P_H(01)$ in the first term on the right-hand side of (H5) for boundary condition TYPE II should read $P_H(10)$.

spondingly a larger η than the values obtained by the alternative formula of Hu (1997*b*).

3. Reflection power ratio profile and diffraction geometry

Using the transfer equations, the reflection power ratio RPR or intensity ratio distribution $P_H[\xi_0, \tau_0, m(n)]/P_0^0$ for a cylindrical crystal (Fig. 1) has been evaluated for the first time as a function of $\sigma_0 X(n) = n \times \Delta n \times \sin 2\theta_B$, where $n = 1, 2, \ldots, n_{\max}$. The RPR profile for a rectangular mosaic distribution, as depicted in Figs. 2 and 3, also offers a unique tool for the investigation of the diffraction geometry.

The diffraction within a cylindrical crystal is a combination of both transmission and reflection geometries as shown in Fig. 1, where **cf** represents the Laue-entrance surface, **fg** the Bragg-entrance and Bragg-exit surface, while **gd** represents the Laue-exit surface. Below, we abbreviate expressions such as 'Laue-entrance and Bragg-exit' by 'Laue–Bragg' *etc*. The projection of point **g** on the $\sigma_0 X$ axis,[4] *i.e.* $\sigma_0 X = 2\tau_0 \sin^2\theta_B$, is an important position for our discussion.

Another important parameter is ξ_0, equal to μ/σ_0 and proportional to $\eta\mu/Q$ in this work, as introduced by Bacon & Lowde (1948), Werner *et al.* (1966) and Hu (1997*a*,*b*) for a plane crystal. ξ_0 is a unique variable suitable for the investigation of the relationship between the diffraction behavior of an absorbing crystal and its physical and geometrical parameters.

All the curves depicted in Fig. 2(*b*) for the absorbing crystal are evaluated at $\xi_0 = 0.5$. At this value, the absorption mean free path (MFP), $1/\mu$, is twice the scattering MFP, $1/\sigma_0$. Thus, in the case of $\tau_0 = 1.0$ and $\mu\rho = 0.5$, the diameter of the cylinder equals two scattering MFP and one absorption MFP; the beam incident on the crystal is then reflected less than three times and absorbed less than once on average before leaving the crystal as reflected beam, and the exit beam originates from almost everywhere on **fgd** of the cylinder. However, when both τ_0 and ξ_0 become large enough, the Bragg–Bragg geometry becomes the dominant part and one may note in Fig. 2(*c*) that, for $\theta_B = 20^\circ$, $\xi_0 = 1$ and $\tau_0 = 5$, the part of the beam emerging beyond point **g**, *i.e.* from $\sigma_0 X > 1.17$, becomes very weak, contributing only 9.6% of the power of the diffracted exit beam. This contribution extinguishes when $\xi_0 = 1$, $\tau_0 > 50$ or $\xi_0 = 2$, $\tau_0 > 30$.

For a sample with given ρ and μ, an increase of η reduces σ_0, τ_0 and increases ξ_0. Taking the $\mu\rho = 2.5$ curves in Figs. 2(*b*) and 2(*c*) as examples, one can see that an increase of ξ_0 from 0.5 to 1.0 results in a decrease of τ_0 from 5.0 to 2.5. This reduces the average number of reflections the exit beam suffers within the crystal and as a result $\mathrm{RPR}^{\mathrm{av}}$ decreases and the asymmetry of the power ratio distribution increases.

The intensity ratio or RPR profile depicted in Figs. 2(*b*) and 2(*c*) can also be explained by the diffraction geometry. For instance, referring to the curves for $\tau_0 > 2.5$, the fast decay of the intensity ratio beyond the position $\sigma_0 X$ corresponding to point **g** in Fig. 1 can easily be explained as a result of the Laue–Laue and Bragg–Laue diffraction geometries. In particular, the very fast rise and decay of the intensity corresponding to the diffraction from **fg** is illustrative. Here the geometry is of the Bragg–Bragg type but with a gradually changing symmetry. One can see from Fig. 1 that, for $\theta_B \leq 45^\circ$, **f** is a point of glancing emergence, while **g** is a point of glancing incidence. Using the terminology of the plane crystal (Hu, 1997*a*), the diffraction geometry parameter b from points **f** and **g** corresponds to a gradual change from $|b| = \infty$ through $b = -1$ to $b = 0$, and the position of the symmetric Bragg case is located midway between **f** and **g**. Thus the space condensation of the diffraction current density, or the Fankuchen (1937) effect, appears around point **f** when $\xi_0 > 0.3$, while at point **g** this effect reverses and space dilution becomes dominant [see equations (11) and (20) of Hu (1997*a*)]. This explains the steep rise and fall of the intensity ratio of the exit beam emerging between **f** and **g** as shown in Figs. 2(*b*) and 2(*c*). Since the angle between the incident beam and the crystal surface around point **f** increases with θ_B, this effect will be more pronounced with increasing θ_B for a sample with given ξ_0 and τ_0.

It seems worthwhile to compare the I_H/I_0 value of the midpoint between **f** and **g** for the symmetric Bragg case of a cylinder with the corresponding I_H/I_0 for a plane crystal. P_H/P_0 for a plane crystal with infinite thickness and symmetric geometry [see equation (12) in Hu (1997*a*)] is

$$P_H/P_0 = I_H/I_0 = 1/[(\xi_0^2 + 2\xi_0)^{1/2} + \xi_0 + 1]. \qquad (20)$$

For $\xi_0 = 1$, one obtains 0.268. The projection of the midpoint between **f** and **g** onto the σX axis, $\tau_0(1 - \cos\theta_B)$, is also an important point in the diffraction geometry. For $\theta_B = 20^\circ$ and $\tau_0 = 5$, it is $5(1 - \cos 20^\circ) = 0.3015$ and the corresponding value of I_H/I_0 for the same ξ_0 at this point is 0.346 (Fig. 2*c*). This value includes the diffraction from a region of about $4/\mu$, or 4 absorption MFP's around **f** containing Bragg–Bragg and Laue–Bragg diffraction geometries producing the Fankuchen effect. I_H/I_0 at the midpoint decreases rapidly at first with increasing τ_0 and then slowly levels off towards the value of 0.277 for $\tau_0 = 50$, $\xi_0 = 1$ and $20 < \theta_B < 45^\circ$. This value deviates by only 3% from the corresponding value for a plane crystal as

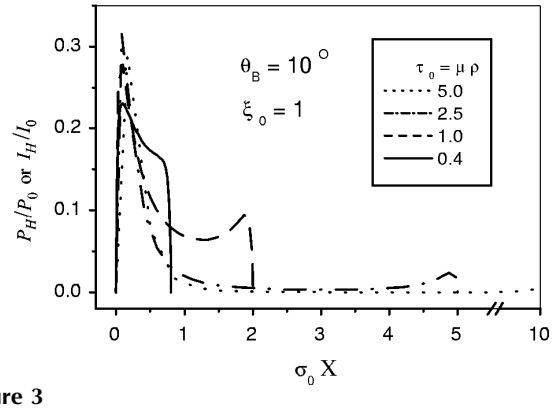

Figure 3
Power ratio distribution for absorbing cylindrical crystals with rectangular mosaic distribution, $\theta_B = 10^\circ$, and four different values of τ_0.

[4] The projection of point **g** on the X axis is $(2\rho/\sin 2\theta_B - \rho/\tan\theta_B) = 2\rho\sin^2\theta_B$.

defined by (20), and the deviation reduces further to 2% when $\xi_0 = 2$ and $\tau_0 = 50$. When τ_0 changes from 5 to 50, the peak values of I_H/I_0 for $\xi_0 = 1$ change from 0.429 to 0.435 for $\theta_B = 20^\circ$, and from 0.432 to 0.451 for $\theta_B = 40^\circ$, respectively. This illustrates the enhancement of the Fankuchen effect with increasing τ_0 or θ_B.

For $\theta_B = 0^\circ$, the diffraction geometry is a pure Laue case: the power ratio goes through a maximum value at a certain thickness of absorbing crystal plate for given ξ_0 (Hu, 1997*a*). For the maximum value and corresponding reduced thickness, see equation (23) and Fig. 4 of that paper. However, owing to the small penetration of the incident beam through the middle part of the cylinder, the RPR profile for the cylinder exhibits a symmetric double peak when $\mu\rho$ is large enough for a given ξ_0. When θ_B increases, the double peak becomes more and more asymmetric and, owing to the absorption, the second peak becomes smaller than the first one and disappears for $\mu\rho \geq 2.5$ as shown in Fig. 3. The areas under the curves are proportional to IRPR. For four different values of $\tau_0 = 0.4$, 1.0, 2.5 and 5.0, they are 0.146, 0.2145, 0.149 and 0.133, respectively. The maximum values are located around $\tau_0 = 1$. This is also shown in Fig. 8(*a*) as a peak close to the $\tau_0 = 1$ position in the $\sigma_0 R_H^\theta/\eta$ *versus* τ_0 curve for a rectangular distribution when $\xi_0 = 1$.

It is also worth noting that the average value of the intensity ratio increases with increasing θ_B or τ_0 for a non-absorbing cylinder and the peak of the intensity ratio distribution curve then extends into a broad plateau with a rather high value when $\tau_0 > 15$ and $\theta_B > 45^\circ$. This phenomenon may offer a possibility for the design of a new type of cylindrical neutron monochromator.

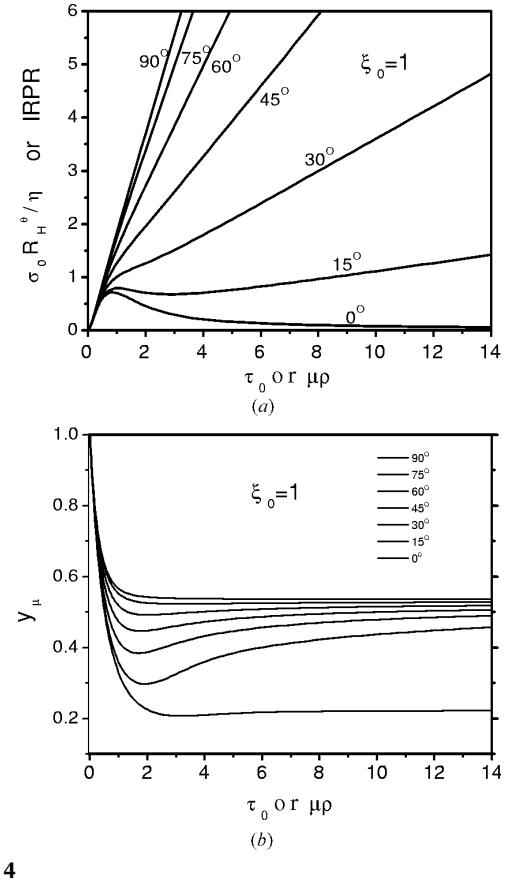

Figure 4
Integrated reflection power ratio IRPR and y_μ for absorbing cylindrical crystals with rectangular mosaic distribution as a function of τ_0 and θ_B. (*a*) IRPR; (*b*) y_μ. The numbers labeling the curves are θ_B.

In the kinematic approximation for a non-absorbing cylindrical crystal, all the power ratio distribution curves RPR_k are half-ellipses, symmetric with respect to the center of the cylinder and with the maximum value of $2\tau_0$ for all θ_B. Hu *et al.* (2001) also published the RPR_k distribution curve for $\theta_B = 20^\circ$, $\mu\rho = 2.5$. This result is quite similar to the transmission profile obtained by Sabine *et al.* (1998) with another method.

4. Relation between the integrated reflection power ratio and the secondary-extinction factor y_μ

From (9), $\mathrm{IRPR} = \sigma_0 R_H^\theta/\eta$ or $\mathrm{IRPR} = 2 \times 3^{1/2} 2\tau_0 \mathrm{RPR}^{\mathrm{av}}$ for a cylindrical crystal with a rectangular mosaic distribution. For a non-absorbing crystal, $\mathrm{RPR}^{\mathrm{av}}$ converges for $\tau_0 \rightarrow \infty$ to 1/2 and 1 for the pure Laue ($\theta_B = 0^\circ$) and Bragg ($\theta_B = 90^\circ$) geometries, respectively. Therefore, corresponding IRPR are $2 \times 3^{1/2}\tau_0$ and $2 \times 3^{1/2} 2\tau_0$. From (18), y_μ is $1/\pi\tau_0$ and $2/\pi\tau_0$, respectively, in agreement with Hamilton (1963).

For an absorbing cylindrical crystal with given ξ_0, IRPR for $\theta_B = 90^\circ$ and $\tau_0 \rightarrow \infty$ can also be obtained as before, but here $\mathrm{RPR}^{\mathrm{av}}$ is identical to P_H/P_0 from (20), thus

$$\sigma_0 R_H^\theta(\xi_0)/\eta = 4 \times 3^{1/2}\tau_0/[(\xi_0^2 + 2\xi_0)^{1/2} + \xi_0 + 1]. \qquad (21)$$

In the kinematic approximation, IRPR_k is $\sigma_0 R_k^\theta/\eta = 2 \times 3^{1/2} \times 2\tau_0/2\xi_0$ [see equation (30) of Hu (1997*a*)]. According to (18), the limiting value of y_μ for $\xi_0 > 0.1$, $\tau_0 \rightarrow \infty$ and $\theta_B = 90^\circ$ is

$$y_\mu(\xi_0) = 2\xi_0/[(\xi_0^2 + 2\xi_0)^{1/2} + \xi_0 + 1]. \qquad (22)$$

The limiting values of y_μ at $\theta_B = 90^\circ$ and at $\xi_0 = 0.5$, 1 and 2 evaluated from (22) are exactly the same as the values shown in Tables 1(*c*), 1(*d*) and 1(*e*), and $y_\mu = 1$ for $\xi_0 \rightarrow \infty$.

For a given ξ_0, the curve of IRPR *versus* the reduced thickness for an infinite plane-parallel absorbing crystal plate is quite different from that of a cylindrical crystal. When the thickness of an absorbing plane crystal increases, IRPR in the Laue case goes over a maximum, while in the Bragg case it approaches a saturation value, which represents the depth of penetration of the radiation in the crystal (see Fig. 6 in Hu, 1997*a*). In a cylindrical crystal, however, IRPR is an integral of the exit diffracted beam over **fgd** of the cylinder. Thus, for low θ_B, the IRPR *versus* τ_0 curve exhibits a peak at a value of τ_0 where the Laue geometry dominates, as shown in Fig. 4(*a*), but if $\theta_B > 25^\circ$ IRPR monotonically increases with τ_0.

All IRPR and y_μ curves for given θ_B but different ξ_0 become rather similar to each other if $\mu\rho = \tau_0\xi_0$ is used as abscissa instead of τ_0. In the following discussion, $\mu\rho$ is used as reference axis.

The case of $\theta_B = 0^\circ$ for a cylindrical crystal represents a pure Laue geometry; however, contrary to the plane crystal plate, there are always some rays passing through the two border

Table 1
Secondary-extinction factor y_μ for cylindrical crystals with a rectangular mosaic distribution as a function of τ_0 and θ_B.

(a) $\xi_0 = 0.0$

$\tau_0\backslash\theta_B$	0°	5°	10°	20°	30°	40°	50°	60°	70°	80°	90°
0.1	0.8486	0.8486	0.8487	0.8492	0.8501	0.8512	0.8525	0.8537	0.8548	0.8554	0.8557
0.2	0.7279	0.7280	0.7284	0.7301	0.7328	0.7363	0.7401	0.7436	0.7463	0.7481	0.7487
0.3	0.6309	0.6311	0.6319	0.6350	0.6399	0.6461	0.6525	0.6582	0.6625	0.6652	0.6661
0.4	0.5522	0.5525	0.5537	0.5583	0.5653	0.5739	0.5827	0.5901	0.5956	0.5991	0.6002
0.5	0.4879	0.4884	0.4899	0.4958	0.5048	0.5155	0.5260	0.5348	0.5412	0.5452	0.5465
0.6	0.4348	0.4353	0.4372	0.4442	0.4549	0.4673	0.4792	0.4888	0.4958	0.5003	0.5017
0.7	0.3905	0.3912	0.3934	0.4014	0.4134	0.4271	0.4400	0.4502	0.4577	0.4624	0.4639
0.8	0.3534	0.3541	0.3565	0.3654	0.3785	0.3931	0.4066	0.4172	0.4249	0.4298	0.4314
0.9	0.3219	0.3227	0.3253	0.3349	0.3488	0.3641	0.3779	0.3887	0.3966	0.4016	0.4033
1.0	0.2951	0.2959	0.2987	0.3088	0.3233	0.3390	0.3530	0.3639	0.3719	0.3769	0.3787
1.1	0.2720	0.2729	0.2758	0.2863	0.3012	0.3171	0.3312	0.3421	0.3500	0.3551	0.3569
1.2	0.2520	0.2529	0.2559	0.2668	0.2819	0.2979	0.3119	0.3227	0.3307	0.3358	0.3375
1.3	0.2345	0.2355	0.2386	0.2496	0.2648	0.2808	0.2947	0.3054	0.3133	0.3184	0.3202
1.4	0.2192	0.2202	0.2233	0.2345	0.2497	0.2656	0.2794	0.2899	0.2977	0.3028	0.3045
1.5	0.2056	0.2066	0.2098	0.2211	0.2363	0.2520	0.2655	0.2759	0.2836	0.2886	0.2904
2.0	0.1565	0.1576	0.1608	0.1718	0.1861	0.2005	0.2128	0.2223	0.2293	0.2340	0.2357
3.0	0.1054	0.1063	0.1092	0.1188	0.1306	0.1423	0.1523	0.1600	0.1658	0.1699	0.1715
4.0	0.0793	0.0802	0.0827	0.0909	0.1007	0.1103	0.1186	0.1251	0.1300	0.1335	0.1348
5.0	0.0635	0.0643	0.0666	0.0736	0.0819	0.0901	0.0972	0.1027	0.1068	0.1099	0.1112
6.0	0.0530	0.0537	0.0557	0.0618	0.0690	0.0761	0.0823	0.0871	0.0907	0.0934	0.0946
7.0	0.0454	0.0461	0.0479	0.0533	0.0596	0.0659	0.0714	0.0756	0.0788	0.0812	0.0823
8.0	0.0397	0.0404	0.0420	0.0468	0.0525	0.0581	0.0630	0.0669	0.0697	0.0718	0.0728
9.0	0.0353	0.0359	0.0374	0.0418	0.0469	0.0519	0.0564	0.0599	0.0625	0.0644	0.0654
10.0	0.0318	0.0323	0.0337	0.0377	0.0424	0.0470	0.0510	0.0543	0.0566	0.0584	0.0593
12.0	0.0265	0.0270	0.0282	0.0315	0.0355	0.0394	0.0429	0.0457	0.0476	0.0491	0.0499
14.0	0.0227	0.0232	0.0242	0.0271	0.0305	0.0340	0.0370	0.0394	0.0411	0.0424	0.0432
16.0	0.0199	0.0203	0.0212	0.0238	0.0268	0.0298	0.0325	0.0347	0.0362	0.0373	0.0380
18.0	0.0177	0.0180	0.0188	0.0212	0.0239	0.0266	0.0290	0.0310	0.0323	0.0333	0.0340
20.0	0.0159	0.0162	0.0170	0.0191	0.0215	0.0240	0.0262	0.0280	0.0292	0.0301	0.0307
25.0	0.0127	0.0130	0.0136	0.0153	0.0173	0.0193	0.0211	0.0225	0.0236	0.0242	0.0247
30.0	0.0106	0.0108	0.0113	0.0128	0.0144	0.0161	0.0176	0.0189	0.0197	0.0203	0.0207

(b) $\xi_0 = 0.2$

$\tau_0\backslash\theta_B$	0°	5°	10°	20°	30°	40°	50°	60°	70°	80°	90°
0.1	0.8487	0.8488	0.8489	0.8495	0.8506	0.8519	0.8535	0.8549	0.8562	0.8570	0.8573
0.2	0.7285	0.7286	0.7293	0.7313	0.7346	0.7388	0.7434	0.7476	0.7509	0.7530	0.7536
0.3	0.6321	0.6324	0.6334	0.6372	0.6432	0.6506	0.6583	0.6651	0.6704	0.6738	0.6749
0.4	0.5541	0.5545	0.5560	0.5616	0.5702	0.5807	0.5912	0.6003	0.6071	0.6115	0.6130
0.5	0.4904	0.4910	0.4929	0.5003	0.5114	0.5245	0.5373	0.5481	0.5562	0.5615	0.5632
0.6	0.4379	0.4387	0.4410	0.4499	0.4632	0.4785	0.4931	0.5052	0.5144	0.5203	0.5223
0.7	0.3943	0.3951	0.3978	0.4081	0.4232	0.4402	0.4562	0.4693	0.4793	0.4858	0.4882
0.8	0.3577	0.3585	0.3617	0.3732	0.3898	0.4082	0.4252	0.4390	0.4497	0.4568	0.4593
0.9	0.3267	0.3277	0.3312	0.3437	0.3616	0.3809	0.3986	0.4131	0.4243	0.4319	0.4347
1.0	0.3003	0.3014	0.3051	0.3186	0.3374	0.3575	0.3757	0.3906	0.4024	0.4104	0.4134
1.1	0.2776	0.2788	0.2827	0.2970	0.3165	0.3372	0.3557	0.3710	0.3832	0.3917	0.3949
1.2	0.2579	0.2592	0.2634	0.2782	0.2983	0.3194	0.3382	0.3538	0.3663	0.3753	0.3787
1.3	0.2408	0.2421	0.2465	0.2619	0.2824	0.3037	0.3228	0.3386	0.3515	0.3609	0.3645
1.4	0.2257	0.2272	0.2317	0.2475	0.2684	0.2899	0.3090	0.3251	0.3383	0.3481	0.3519
1.5	0.2124	0.2140	0.2186	0.2348	0.2559	0.2775	0.2967	0.3129	0.3265	0.3366	0.3407
2.0	0.1644	0.1661	0.1713	0.1886	0.2102	0.2317	0.2510	0.2679	0.2829	0.2948	0.2998
3.0	0.1147	0.1167	0.1226	0.1409	0.1622	0.1831	0.2024	0.2204	0.2376	0.2521	0.2586
4.0	0.0897	0.0922	0.0986	0.1177	0.1391	0.1598	0.1793	0.1981	0.2166	0.2326	0.2400
5.0	0.0750	0.0779	0.0851	0.1053	0.1271	0.1479	0.1677	0.1870	0.2060	0.2227	0.2305
6.0	0.0656	0.0689	0.0770	0.0986	0.1210	0.1421	0.1621	0.1815	0.2005	0.2171	0.2253
7.0	0.0592	0.0631	0.0722	0.0954	0.1185	0.1398	0.1597	0.1790	0.1976	0.2139	0.2222
8.0	0.0548	0.0593	0.0695	0.0944	0.1182	0.1396	0.1593	0.1781	0.1961	0.2119	0.2202
9.0	0.0516	0.0569	0.0684	0.0950	0.1193	0.1405	0.1599	0.1781	0.1954	0.2106	0.2189
10.0	0.0494	0.0556	0.0684	0.0967	0.1213	0.1422	0.1611	0.1787	0.1951	0.2098	0.2181
12.0	0.0468	0.0551	0.0708	0.1019	0.1264	0.1465	0.1642	0.1804	0.1954	0.2089	0.2170
14.0	0.0458	0.0565	0.0752	0.1080	0.1318	0.1508	0.1674	0.1823	0.1960	0.2086	0.2163
16.0	0.0457	0.0590	0.0805	0.1141	0.1369	0.1549	0.1703	0.1841	0.1967	0.2084	0.2159
18.0	0.0460	0.0623	0.0861	0.1196	0.1414	0.1584	0.1729	0.1857	0.1974	0.2084	0.2157
20.0	0.0464	0.0658	0.0914	0.1244	0.1453	0.1615	0.1752	0.1872	0.1981	0.2084	0.2155
25.0	0.0476	0.0744	0.1027	0.1338	0.1532	0.1678	0.1798	0.1901	0.1996	0.2086	0.2152
30.0	0.0483	0.0821	0.1112	0.1409	0.1591	0.1724	0.1831	0.1923	0.2008	0.2089	0.2150

Table 1 (continued)

(*c*) $\xi_0 = 0.5$

$\tau_0\backslash\theta_B$	0°	5°	10°	20°	30°	40°	50°	60°	70°	80°	90°
0.1	0.8490	0.8491	0.8493	0.8500	0.8513	0.8530	0.8549	0.8568	0.8583	0.8593	0.8597
0.2	0.7296	0.7297	0.7305	0.7331	0.7372	0.7425	0.7482	0.7534	0.7576	0.7603	0.7611
0.3	0.6341	0.6345	0.6357	0.6406	0.6483	0.6576	0.6673	0.6759	0.6826	0.6870	0.6885
0.4	0.5571	0.5577	0.5597	0.5670	0.5782	0.5915	0.6048	0.6163	0.6253	0.6312	0.6332
0.5	0.4945	0.4952	0.4979	0.5077	0.5223	0.5391	0.5554	0.5693	0.5802	0.5875	0.5901
0.6	0.4431	0.4441	0.4473	0.4594	0.4770	0.4967	0.5155	0.5314	0.5441	0.5527	0.5559
0.7	0.4005	0.4016	0.4056	0.4198	0.4401	0.4624	0.4831	0.5008	0.5150	0.5248	0.5285
0.8	0.3649	0.3663	0.3707	0.3870	0.4096	0.4340	0.4564	0.4755	0.4910	0.5021	0.5062
0.9	0.3348	0.3364	0.3415	0.3596	0.3842	0.4102	0.4340	0.4543	0.4712	0.4833	0.4879
1.0	0.3093	0.3112	0.3167	0.3365	0.3630	0.3904	0.4153	0.4367	0.4547	0.4678	0.4728
1.1	0.2875	0.2895	0.2956	0.3170	0.3450	0.3735	0.3994	0.4218	0.4408	0.4549	0.4603
1.2	0.2687	0.2708	0.2774	0.3003	0.3296	0.3592	0.3858	0.4091	0.4291	0.4440	0.4499
1.3	0.2523	0.2547	0.2617	0.2860	0.3165	0.3469	0.3743	0.3983	0.4191	0.4348	0.4411
1.4	0.2380	0.2406	0.2481	0.2737	0.3053	0.3364	0.3644	0.3891	0.4107	0.4271	0.4337
1.5	0.2255	0.2282	0.2363	0.2631	0.2957	0.3274	0.3559	0.3813	0.4035	0.4205	0.4274
2.0	0.1809	0.1846	0.1950	0.2275	0.2640	0.2980	0.3284	0.3557	0.3802	0.3993	0.4072
3.0	0.1379	0.1440	0.1600	0.2028	0.2443	0.2801	0.3112	0.3389	0.3636	0.3833	0.3922
4.0	0.1201	0.1297	0.1523	0.2043	0.2478	0.2826	0.3118	0.3373	0.3598	0.3783	0.3873
5.0	0.1130	0.1271	0.1572	0.2156	0.2581	0.2902	0.3167	0.3395	0.3595	0.3764	0.3853
6.0	0.1109	0.1308	0.1681	0.2292	0.2689	0.2982	0.3221	0.3425	0.3603	0.3756	0.3842
7.0	0.1113	0.1376	0.1810	0.2418	0.2784	0.3052	0.3269	0.3453	0.3613	0.3753	0.3836
8.0	0.1125	0.1457	0.1936	0.2524	0.2864	0.3111	0.3310	0.3478	0.3623	0.3752	0.3832
9.0	0.1140	0.1541	0.2050	0.2610	0.2930	0.3161	0.3345	0.3499	0.3633	0.3753	0.3830
10.0	0.1152	0.1622	0.2147	0.2682	0.2986	0.3204	0.3376	0.3518	0.3643	0.3754	0.3828
12.0	0.1169	0.1769	0.2301	0.2796	0.3075	0.3271	0.3423	0.3549	0.3658	0.3757	0.3825
14.0	0.1179	0.1894	0.2417	0.2884	0.3144	0.3323	0.3460	0.3572	0.3670	0.3760	0.3824
16.0	0.1185	0.2002	0.2508	0.2955	0.3200	0.3364	0.3488	0.3591	0.3680	0.3762	0.3823
18.0	0.1188	0.2094	0.2584	0.3015	0.3245	0.3397	0.3511	0.3605	0.3688	0.3765	0.3822
20.0	0.1191	0.2175	0.2650	0.3065	0.3282	0.3424	0.3530	0.3618	0.3695	0.3767	0.3822
25.0	0.1194	0.2335	0.2782	0.3166	0.3355	0.3476	0.3566	0.3641	0.3708	0.3772	0.3821
30.0	0.1196	0.2456	0.2883	0.3237	0.3405	0.3511	0.3590	0.3657	0.3717	0.3775	0.3821

(*d*) $\xi_0 = 1.0$

$\tau_0\backslash\theta_B$	0°	5°	10°	20°	30°	40°	50°	60°	70°	80°	90°
0.1	0.8496	0.8496	0.8499	0.8509	0.8527	0.8549	0.8575	0.8599	0.8619	0.8633	0.8637
0.2	0.7313	0.7315	0.7326	0.7362	0.7419	0.7490	0.7564	0.7633	0.7688	0.7725	0.7737
0.3	0.6376	0.6382	0.6399	0.6469	0.6575	0.6701	0.6829	0.6942	0.7033	0.7093	0.7115
0.4	0.5626	0.5635	0.5663	0.5770	0.5928	0.6108	0.6284	0.6437	0.6560	0.6643	0.6673
0.5	0.5021	0.5034	0.5074	0.5220	0.5428	0.5657	0.5874	0.6061	0.6212	0.6317	0.6355
0.6	0.4530	0.4545	0.4597	0.4784	0.5039	0.5311	0.5562	0.5778	0.5954	0.6077	0.6123
0.7	0.4126	0.4147	0.4210	0.4436	0.4736	0.5044	0.5323	0.5562	0.5759	0.5899	0.5952
0.8	0.3793	0.3819	0.3895	0.4160	0.4500	0.4839	0.5140	0.5399	0.5613	0.5766	0.5824
0.9	0.3517	0.3547	0.3636	0.3940	0.4316	0.4681	0.5000	0.5274	0.5502	0.5666	0.5729
1.0	0.3285	0.3320	0.3423	0.3765	0.4174	0.4559	0.4893	0.5178	0.5416	0.5589	0.5657
1.1	0.3090	0.3131	0.3248	0.3629	0.4066	0.4469	0.4813	0.5106	0.5352	0.5531	0.5602
1.2	0.2925	0.2972	0.3104	0.3522	0.3985	0.4401	0.4752	0.5052	0.5302	0.5486	0.5560
1.3	0.2786	0.2838	0.2986	0.3440	0.3927	0.4352	0.4709	0.5011	0.5264	0.5451	0.5527
1.4	0.2667	0.2726	0.2891	0.3381	0.3887	0.4319	0.4678	0.4981	0.5235	0.5423	0.5501
1.5	0.2566	0.2632	0.2814	0.3338	0.3861	0.4298	0.4657	0.4959	0.5212	0.5401	0.5480
2.0	0.2246	0.2355	0.2633	0.3311	0.3875	0.4303	0.4643	0.4924	0.5159	0.5341	0.5422
3.0	0.2069	0.2308	0.2798	0.3619	0.4124	0.4475	0.4746	0.4968	0.5154	0.5307	0.5386
4.0	0.2093	0.2502	0.3144	0.3920	0.4335	0.4622	0.4842	0.5021	0.5172	0.5300	0.5374
5.0	0.2139	0.2727	0.3433	0.4120	0.4478	0.4725	0.4913	0.5064	0.5191	0.5300	0.5368
6.0	0.2169	0.2928	0.3640	0.4258	0.4581	0.4800	0.4964	0.5096	0.5207	0.5303	0.5365
7.0	0.2186	0.3099	0.3792	0.4362	0.4660	0.4857	0.5004	0.5121	0.5219	0.5305	0.5364
8.0	0.2196	0.3246	0.3909	0.4446	0.4722	0.4902	0.5035	0.5141	0.5230	0.5308	0.5363
9.0	0.2202	0.3371	0.4004	0.4514	0.4772	0.4939	0.5060	0.5156	0.5238	0.5310	0.5362
10.0	0.2206	0.3479	0.4085	0.4573	0.4816	0.4970	0.5081	0.5170	0.5246	0.5313	0.5361
12.0	0.2211	0.3654	0.4215	0.4665	0.4881	0.5016	0.5113	0.5191	0.5257	0.5316	0.5361
14.0	0.2214	0.3790	0.4318	0.4736	0.4931	0.5050	0.5136	0.5206	0.5265	0.5319	0.5360
16.0	0.2216	0.3900	0.4403	0.4792	0.4969	0.5076	0.5154	0.5217	0.5272	0.5322	0.5360
18.0	0.2218	0.3991	0.4473	0.4837	0.4999	0.5097	0.5168	0.5226	0.5277	0.5324	0.5360
20.0	0.2218	0.4069	0.4533	0.4874	0.5023	0.5114	0.5179	0.5233	0.5281	0.5325	0.5360
25.0	0.2220	0.4223	0.4650	0.4945	0.5070	0.5145	0.5201	0.5247	0.5289	0.5328	0.5359
30.0	0.2221	0.4342	0.4735	0.4992	0.5100	0.5165	0.5214	0.5256	0.5294	0.5330	0.5359

Table 1 (continued)

(*e*) $\xi_0 = 2.0$

$\tau_0\backslash\theta_B$	0°	5°	10°	20°	30°	40°	50°	60°	70°	80°	90°
0.1	0.8506	0.8507	0.8513	0.8529	0.8556	0.8590	0.8627	0.8663	0.8692	0.8712	0.8717
0.2	0.7351	0.7357	0.7372	0.7431	0.7520	0.7626	0.7734	0.7832	0.7911	0.7965	0.7983
0.3	0.6455	0.6464	0.6496	0.6614	0.6783	0.6972	0.7152	0.7310	0.7436	0.7522	0.7553
0.4	0.5755	0.5773	0.5825	0.6015	0.6270	0.6536	0.6777	0.6982	0.7146	0.7258	0.7300
0.5	0.5209	0.5235	0.5313	0.5584	0.5923	0.6253	0.6540	0.6778	0.6968	0.7099	0.7149
0.6	0.4781	0.4818	0.4927	0.5284	0.5699	0.6079	0.6395	0.6654	0.6859	0.7002	0.7057
0.7	0.4448	0.4499	0.4641	0.5087	0.5567	0.5979	0.6312	0.6580	0.6792	0.6942	0.7001
0.8	0.4191	0.4256	0.4437	0.4970	0.5502	0.5932	0.6270	0.6539	0.6752	0.6903	0.6964
0.9	0.3993	0.4075	0.4299	0.4916	0.5483	0.5919	0.6253	0.6517	0.6727	0.6878	0.6941
1.0	0.3843	0.3946	0.4215	0.4909	0.5497	0.5929	0.6253	0.6509	0.6712	0.6861	0.6924
1.1	0.3733	0.3857	0.4175	0.4936	0.5530	0.5951	0.6263	0.6508	0.6704	0.6849	0.6912
1.2	0.3654	0.3803	0.4170	0.4985	0.5575	0.5980	0.6278	0.6513	0.6700	0.6841	0.6904
1.3	0.3599	0.3776	0.4193	0.5049	0.5626	0.6012	0.6296	0.6519	0.6698	0.6834	0.6897
1.4	0.3564	0.3771	0.4236	0.5120	0.5678	0.6046	0.6316	0.6527	0.6698	0.6830	0.6892
1.5	0.3545	0.3782	0.4295	0.5194	0.5730	0.6079	0.6335	0.6537	0.6699	0.6827	0.6888
2.0	0.3564	0.3977	0.4669	0.5517	0.5941	0.6217	0.6421	0.6582	0.6713	0.6819	0.6877
3.0	0.3673	0.4449	0.5228	0.5869	0.6181	0.6384	0.6532	0.6647	0.6741	0.6820	0.6869
4.0	0.3712	0.4802	0.5518	0.6053	0.6313	0.6478	0.6596	0.6687	0.6761	0.6824	0.6866
5.0	0.3727	0.5059	0.5699	0.6174	0.6399	0.6538	0.6636	0.6712	0.6775	0.6827	0.6865
6.0	0.3735	0.5251	0.5829	0.6262	0.6460	0.6580	0.6665	0.6730	0.6784	0.6831	0.6864
7.0	0.3739	0.5397	0.5930	0.6328	0.6504	0.6611	0.6686	0.6744	0.6792	0.6833	0.6864
8.0	0.3742	0.5513	0.6012	0.6379	0.6539	0.6635	0.6702	0.6754	0.6798	0.6835	0.6864
9.0	0.3743	0.5607	0.6080	0.6421	0.6567	0.6653	0.6714	0.6762	0.6802	0.6837	0.6864
10.0	0.3745	0.5686	0.6138	0.6456	0.6590	0.6670	0.6725	0.6769	0.6806	0.6839	0.6863
12.0	0.3746	0.5813	0.6229	0.6508	0.6625	0.6693	0.6741	0.6779	0.6812	0.6841	0.6863
14.0	0.3747	0.5914	0.6298	0.6547	0.6649	0.6709	0.6752	0.6786	0.6816	0.6842	0.6863
16.0	0.3748	0.5996	0.6352	0.6576	0.6668	0.6721	0.6760	0.6791	0.6818	0.6844	0.6863
18.0	0.3748	0.6062	0.6395	0.6600	0.6682	0.6731	0.6766	0.6795	0.6820	0.6844	0.6863
20.0	0.3749	0.6119	0.6431	0.6618	0.6694	0.6738	0.6771	0.6798	0.6822	0.6845	0.6863
25.0	0.3749	0.6228	0.6499	0.6654	0.6716	0.6753	0.6780	0.6804	0.6826	0.6847	0.6863
30.0	0.3749	0.6306	0.6545	0.6676	0.6729	0.6761	0.6786	0.6807	0.6828	0.6848	0.6863

regions of the absorbing sample when $\mu\rho$ is large. This explains why $y_\mu \neq 0$ in such a case as shown in Fig. 4(*b*).

When $0 < \theta_B \leq 45^\circ$ and $\mu\rho \leq 0.5$, y_μ drops very quickly with increasing $\mu\rho$. For $0 < \theta_B < 20^\circ$ and $\xi_0 > 0.8$, both IRPR and y_μ increase after a dip located around $\mu\rho$ of 2 to 4, the interval where the diffraction geometry changes gradually from the Laue to the Bragg case. Since the central angle extended by **fg** is $2\theta_B$, the projection of **g** on the $\sigma_0 X$ axis is proportional to $\sin^2\theta_B$[5] and the rate of change from the Laue to the Bragg case increases with θ_B and $\mu\rho$. Thus, the rate of increase of y_μ reduces sharply with decreasing θ_B and severe extinction appears at small θ_B when $\mu\rho > 5$. With increasing $\mu\rho$, the relationship between IRPR and θ_B approaches the $\sin^2\theta_B$ law because of a concomitant strong reduction of the non-Bragg–Bragg component in the exit beam. For instance, the ratio of the IRPR values at $\theta_B = 30$ and 15° is 3.43 for $\mu\rho = 14$. This ratio deviates by only 8.7% from the value of 3.73 for the $\sin^2\theta_B$ approximation, and by only 1.5% at $\mu\rho = 30$. Finally, when $\mu\rho$ is very large, IRPR at given θ_B and ξ_0 assumes the value from (21) multiplied by $\sin^2\theta_B$.

When $\theta_B = 90^\circ$, IRPR and y_μ for $\mu\rho = 30$ become identical with the values for $\mu\rho \rightarrow \infty$ calculated from (21) and (22), respectively. For $\mu\rho \rightarrow \infty$, all the values of y_μ for other curves at $\theta_B \neq 0^\circ$ are slightly smaller than at $\theta_B = 90^\circ$. This small difference can be explained by comparing the absorbing cylindrical crystal at large $\mu\rho$ with a plane crystal. In the plane crystal, y_μ for the symmetric Bragg case with $b = -1$ is always slightly larger than for the asymmetric case $|b| \neq 1$ (Fig. 4 in Hu, 1997*b*). Compared with a cylinder with very large $\mu\rho$, the diffraction geometry is essentially that of the Bragg–Bragg case, restricted to the **fg** region but with continuously changing b as described before. Take $\theta_B = 40^\circ$ and $\xi_0 = 2$ as an example. One finds that, for $\mu\rho > 100$, y_μ takes the value 0.6776, slightly smaller than 0.6858 for a plane crystal in symmetric diffraction calculated by (22).

For $45 < \theta_B \leq 90^\circ$, the **gd** region corresponding to the Bragg–Laue case decreases with increasing θ_B until all of the incidence surface **cfg** contributes to the exit beam at $\theta_B = 90^\circ$ for any value of ξ_0.

5. Secondary-extinction factor and transmission coefficient A^*

5.1. Secondary-extinction factor

Fig. 5 shows a three-dimensional plot of y_μ *versus* τ_0 and ξ_0 for $\theta_B = 20^\circ$. The iso-extinction-factor contours y_μ = constant are shown as white curves. We note that at $\xi_0 = 0$ y_μ decreases monotonically with increasing τ_0. A dip appears in the y_μ *versus* τ_0 curves whose position shifts toward smaller τ_0 with

[5] See footnote 4.

increasing ξ_0. For ξ_0 = 1, 2 and 3, the corresponding positions of the dip are τ_0 = 1.85, 0.95, 0.75 and the y_μ values at the dip are 0.331, 0.491 and 0.591, respectively.

Fig. 6 shows the three-dimensional dependence of y_μ on θ_B and ξ_0 for a constant reduced radius of the cylinder τ_0 = 5. Note that the extinction is large for non-absorbing crystals. For given θ_B and τ_0, y_μ increases with ξ_0 and the shapes of the y_μ *versus* θ_B curves change considerably. A large decrease of the extinction factor y_μ with decreasing θ_B from 15 to 0° appears for $20 > \xi_0 > 0.1$ and the rate of change increases with ξ_0 or τ_0.

The calculated y_μ for cylindrical crystals with rectangular mosaic distribution as a function of τ_0 and θ_B are listed in Tables 1(*a*)–(*e*) for different ξ_0, and the ξ_0 = 1 case is also illustrated in Fig. 4(*b*). The number of grid points used for the calculation are: n_0 = 7200 for θ_B = 0 and 90°; n_0 = 4000 for θ_B = 5° and n_0 = 4000, 5000 and 6000 for θ_B between 10 and 80° and τ_0 = 0.1–2, 3–9 and 10–30, respectively. Since $n_{\max} = n_0/\sin 2\theta_B$, the actual numbers used are even larger, *e.g.* for θ_B = 5°, $n_{\max}$ = 4000/sin 10° = 23035. The accuracy of y_μ increases with increasing θ_B. The accuracy of y_μ is lowest at τ_0 = 15 and $\theta_B \geq 10°$ (0.02%), and improves to 0.004% when θ_B = 80°.

The reciprocal secondary-extinction factor for a non-absorbing cylinder has been calculated by Hamilton (1963). He used grid sizes of $2\rho/120$ for $22.5 < \theta_B < 67.5°$, $2\rho/80$ for θ_B = 11.25 and 78.75°. In order to compare our results with his work, $n_{\max}$ = 4000/sin $2\theta_B$ was used in the calculation. For θ_B = 0 and 90°, our values of y_μ^{-1} are exactly the same as those of Hamilton when the grid size is $2\rho/360$. For the other angles, the maximum deviation is less than 0.015% and 0.55% for $2\tau_0$ = 1 and 6, respectively. For $2\tau_0$ = 30, y_μ^{-1} is 43.73, 38.29, 33.59, 30.08, 27.69, 26.20 and 25.28 for θ_B = 11.25, 22.5, 33.75, 45, 56.25, 67.5 and 78.75°, respectively. The maximum deviation is +1.55% at 22.5° where Hamilton's value is 37.70. For larger θ_B, the deviation decreases and becomes −0.24% for θ_B = 78.75°.

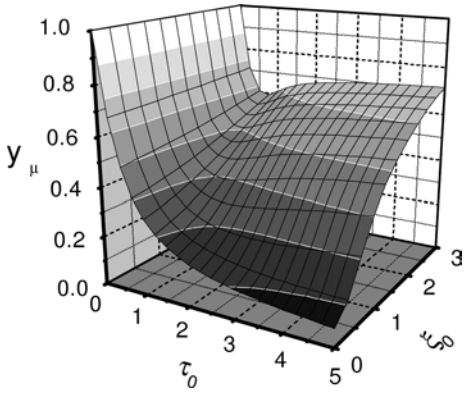

Figure 5
Secondary-extinction factor y_μ at θ_B = 20° for cylindrical crystals with the rectangular mosaic distribution as a function of τ_0 and ξ_0.

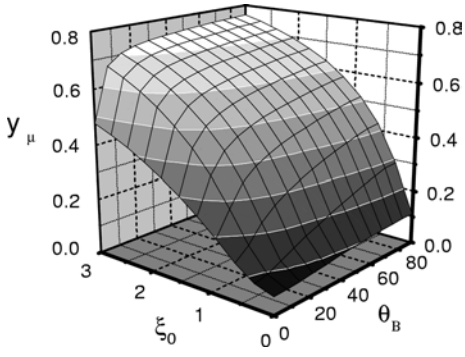

Figure 6
Secondary-extinction factor y_μ for cylindrical crystals with rectangular mosaic distribution as a function of ξ_0 and θ_B (°) at τ_0 = 5.0.

5.2. Transmission coefficient A*

As a complement to Table 6.3.3.2 in Vol. C of *International Tables for Crystallography* (Maslen, 1995, here referred to as *ITCr*) and in order to check the accuracy of y_μ, the transmission coefficients $A^* = 1/A$ for cylinders with strong absorption, $\mu\rho$ from 2.6 to 30 and θ_B from 0 to 40° and from 45 to 90°, are calculated using the formula for A^* [equation (6.3.3.4) in *ITCr*], and listed in Table 2. In this calculation, ρ and the angle 2π are divided equally into n parts: $\Delta\rho = \rho/n$ and angle $\Delta\varphi = 2\pi/n$, n = 3000 for $\mu\rho$ = 2.6 and 2.8, n = 4000 for $\mu\rho$ = 3 to 9.8, n = 6000 to 10000 for $\mu\rho$ = 10.0 to 30. The lowest accuracy of A^* is 0.06%. The results are more accurate than the numbers listed in Vol. II of *International Tables for X-ray Crystallography* (1972) (here referred to as *ITXCr*), particularly for $\mu\rho \geq 15$, θ_B = 5 and 15°. The results obtained for $\mu\rho$ = 2.5 are in exact agreement with the corresponding values listed in *ITCr*. In order to estimate the accuracy of y_μ, A^* calculated with precision 10^{-6} for $\mu\rho$ = 3 and 20 using the method of Thorkildsen & Larsen (1998*b*) is listed in Table 3 (calc. A). Another independent set of A^* values is obtained from y_μ of (15) and (17), *i.e.* the denominator of (18). These numbers of A^* are also listed in Table 3 (calc. B). Note that the accuracy of y_μ for the same $\mu\rho$ is higher than that of Dev. B in Table 3 since in the evaluation of y_μ both the numerator and the denominator are calculated by Euler's method and possess the same systematic deviation, and thus the accuracy is

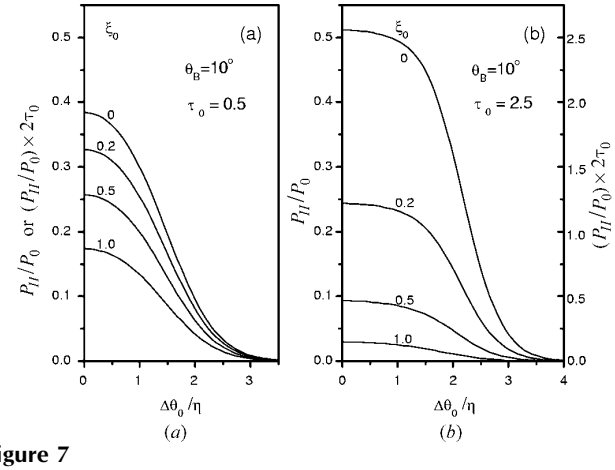

Figure 7
Rocking curves of P_H/P_0 and $(P_H/P_0) \times 2\tau_0$ for a cylindrical crystal with a Gaussian mosaic distribution at different values of ξ_0. (*a*) τ_0 = 0.5; (*b*) τ_0 = 2.5.

Table 2
Transmission coefficient A^* for successive values of θ_B; cylinders.

$\mu\rho$	0°	5°	10°	15°	20°	25°	30°	35°	40°	$\mu\rho$
2.6	45.08	43.32	38.90	33.56	28.53	24.28	20.84	18.10	15.92	2.6
2.8	56.53	53.85	47.37	39.93	33.25	27.84	23.60	20.29	17.69	2.8
3.0	70.11	66.17	56.94	46.87	38.27	31.56	26.43	22.52	19.50	3.0
3.2	86.05	80.36	67.57	54.33	43.54	35.40	29.35	24.80	21.34	3.2
3.4	104.54	96.53	79.22	62.24	49.01	39.35	32.31	27.12	23.20	3.4
3.6	125.74	114.71	91.84	70.56	54.67	43.38	35.33	29.46	25.08	3.6
3.8	149.84	134.94	105.36	79.23	60.47	47.49	38.39	31.83	26.97	3.8
4.0	176.97	157.23	119.70	88.20	66.39	51.66	41.48	34.22	28.88	4.0
4.2	207.29	181.57	134.80	97.43	72.43	55.89	44.60	36.63	30.80	4.2
4.4	240.92	207.94	150.60	106.90	78.57	60.16	47.75	39.05	32.73	4.4
4.6	278.00	236.32	167.02	116.57	84.78	64.48	50.93	41.49	34.67	4.6
4.8	318.67	266.67	184.01	126.42	91.08	68.84	54.13	43.94	36.62	4.8
5.0	363.04	298.97	201.54	136.44	97.44	73.23	57.34	46.40	38.57	5.0
5.2	411.25	333.16	219.55	146.61	103.88	77.65	60.58	48.88	40.53	5.2
5.4	463.43	369.21	238.01	156.92	110.37	82.11	63.83	51.36	42.50	5.4
5.6	519.71	407.09	256.89	167.37	116.92	86.59	67.10	53.86	44.48	5.6
5.8	580.24	446.74	276.17	177.94	123.52	91.11	70.38	56.36	46.46	5.8
6.0	645.15	488.14	295.82	188.63	130.18	95.64	73.68	58.87	48.44	6.0
6.2	714.59	531.24	315.82	199.43	136.88	100.21	76.99	61.39	50.43	6.2
6.4	788.70	576.00	336.15	210.34	143.63	104.79	80.31	63.91	52.42	6.4
6.6	867.62	622.38	356.79	221.36	150.43	109.40	83.64	66.44	54.42	6.6
6.8	951.51	670.35	377.74	232.47	157.26	114.02	86.98	68.98	56.42	6.8
7.0	1040.50	719.85	398.98	243.67	164.14	118.67	90.34	71.53	58.42	7.0
7.2	1134.80	770.87	420.49	254.96	171.05	123.33	93.70	74.07	60.42	7.2
7.4	1234.50	823.34	442.26	266.34	178.01	128.01	97.07	76.63	62.43	7.4
7.6	1339.70	877.24	464.29	277.81	184.99	132.71	100.45	79.18	64.44	7.6
7.8	1450.70	932.53	486.57	289.35	192.01	137.42	103.84	81.75	66.46	7.8
8.0	1567.50	989.16	509.07	300.96	199.05	142.15	107.24	84.31	68.48	8.0
8.2	1690.30	1047.10	531.81	312.65	206.13	146.88	110.64	86.88	70.50	8.2
8.4	1819.30	1106.30	554.76	324.41	213.23	151.64	114.04	89.46	72.52	8.4
8.6	1954.70	1166.80	577.92	336.23	220.36	156.40	117.46	92.03	74.54	8.6
8.8	2096.50	1228.40	601.28	348.12	227.52	161.18	120.88	94.61	76.56	8.8
9.0	2244.90	1291.30	624.84	360.07	234.70	165.96	124.31	97.19	78.59	9.0
9.2	2400.10	1355.20	648.59	372.08	241.90	170.76	127.74	99.78	80.62	9.2
9.4	2562.20	1420.30	672.52	384.14	249.12	175.56	131.17	102.37	82.65	9.4
9.6	2731.40	1486.40	696.62	396.26	256.36	180.38	134.61	104.96	84.68	9.6
9.8	2907.80	1553.60	720.89	408.43	263.63	185.20	138.06	107.55	86.71	9.8
10.0	3091.60	1621.90	745.33	420.65	270.91	190.04	141.51	110.15	88.75	10.0
11.0	4127.90	1977.00	869.82	482.41	307.58	214.31	158.81	123.16	98.93	11.0
12.0	5371.00	2353.60	997.68	545.15	344.61	238.74	176.19	136.21	109.14	12.0
13.0	6838.90	2748.80	1128.50	608.68	381.92	263.31	193.63	149.29	119.37	13.0
14.0	8551.00	3160.40	1261.70	672.88	419.48	287.97	211.13	162.40	129.62	14.0
15.0	10527.00	3586.70	1397.10	737.64	457.24	312.72	228.66	175.54	139.88	15.0
16.0	12787.00	4026.30	1534.30	802.88	495.16	337.54	246.23	188.69	150.15	16.0
17.0	15356.00	4478.70	1673.20	868.54	533.24	362.43	263.83	201.86	160.43	17.0
18.0	18226.60	4940.70	1813.40	934.51	571.42	387.36	281.45	215.04	170.71	18.0
19.0	21470.00	5413.40	1954.90	1000.80	609.72	412.34	299.10	228.23	181.00	19.0
20.0	25025.00	5894.30	2097.50	1067.40	648.09	437.35	316.77	241.43	191.30	20.0
21.0	28970.00	6383.60	2241.20	1134.20	686.57	462.41	334.45	254.64	201.60	21.0
22.0	33285.00	6879.90	2385.40	1201.20	725.09	487.48	352.14	267.86	211.91	22.0
23.0	38070.00	7384.50	2530.60	1268.40	763.69	512.59	369.85	281.08	222.22	23.0
24.0	43249.00	7894.80	2676.50	1335.70	802.34	537.72	387.57	294.32	232.53	24.0
25.0	48880.00	8411.20	2823.00	1403.20	841.03	562.86	405.29	307.55	242.85	25.0
26.0	54978.00	8932.80	2970.10	1470.80	879.77	588.03	423.03	320.79	253.17	26.0
27.0	61591.00	9459.50	3117.70	1538.50	918.55	613.21	440.77	334.03	263.49	27.0
28.0	68701.00	9991.80	3265.90	1606.30	957.36	638.41	458.52	347.28	273.81	28.0
29.0	76298.00	10528.00	3414.30	1674.30	996.21	663.61	476.27	360.53	284.14	29.0
30.0	84521.00	11068.00	3563.20	1742.30	1035.10	688.83	494.04	373.78	294.46	30.0

improved while, for A^*, such a systematic deviation cannot be reduced through the division of (15) by an exact value of $V = \pi\rho^2 h$.

IRPR values for cylindrical crystals with a rectangular mosaic distribution can be obtained as follows from y_μ listed in Table 1 and A^* listed in Table 2. For given θ_B, $\mu\rho$ and ξ_0, τ_0 is

Table 2 (continued)

$\mu\rho$	45°	50°	55°	60°	65°	70°	75°	80°	85°	90°	$\mu\rho$
2.6	14.16	12.75	11.61	10.68	9.927	9.327	8.863	8.526	8.318	8.247	2.6
2.8	15.64	14.01	12.69	11.63	10.77	10.09	9.568	9.187	8.950	8.869	2.8
3.0	17.14	15.27	13.78	12.59	11.63	10.86	10.28	9.849	9.584	9.492	3.0
3.2	18.66	16.56	14.89	13.55	12.48	11.64	10.99	10.51	10.22	10.12	3.2
3.4	20.19	17.85	15.99	14.52	13.35	12.41	11.70	11.18	10.85	10.74	3.4
3.6	21.74	19.15	17.11	15.49	14.21	13.19	12.41	11.85	11.49	11.36	3.6
3.8	23.30	20.46	18.23	16.47	15.08	13.98	13.13	12.51	12.13	11.99	3.8
4.0	24.86	21.77	19.36	17.45	15.95	14.76	13.85	13.18	12.76	12.62	4.0
4.2	26.43	23.09	20.49	18.44	16.82	15.55	14.56	13.85	13.40	13.24	4.2
4.4	28.01	24.41	21.62	19.42	17.69	16.33	15.28	14.52	14.04	13.87	4.4
4.6	29.60	25.74	22.75	20.41	18.57	17.12	16.00	15.19	14.68	14.49	4.6
4.8	31.19	27.07	23.89	21.40	19.44	17.91	16.73	15.86	15.31	15.12	4.8
5.0	32.79	28.41	25.03	22.40	20.32	18.70	17.45	16.53	15.95	15.75	5.0
5.2	34.39	29.75	26.17	23.39	21.20	19.49	18.17	17.21	16.59	16.37	5.2
5.4	35.99	31.09	27.32	24.38	22.08	20.28	18.89	17.88	17.23	17.00	5.4
5.6	37.60	32.43	28.47	25.38	22.96	21.07	19.62	18.55	17.87	17.63	5.6
5.8	39.21	33.78	29.61	26.38	23.84	21.86	20.34	19.23	18.51	18.25	5.8
6.0	40.83	35.13	30.76	27.38	24.73	22.66	21.07	19.90	19.15	18.88	6.0
6.2	42.45	36.47	31.91	28.38	25.61	23.45	21.79	20.57	19.79	19.51	6.2
6.4	44.07	37.83	33.06	29.38	26.49	24.25	22.52	21.25	20.43	20.14	6.4
6.6	45.69	39.18	34.22	30.38	27.38	25.04	23.24	21.92	21.07	20.76	6.6
6.8	47.31	40.53	35.37	31.38	28.26	25.83	23.97	22.60	21.71	21.39	6.8
7.0	48.94	41.89	36.52	32.38	29.15	26.63	24.69	23.27	22.35	22.02	7.0
7.2	50.57	43.24	37.68	33.38	30.03	27.43	25.42	23.95	23.00	22.65	7.2
7.4	52.20	44.60	38.83	34.38	30.92	28.22	26.15	24.62	23.64	23.27	7.4
7.6	53.83	45.96	39.99	35.39	31.81	29.02	26.88	25.30	24.28	23.90	7.6
7.8	55.47	47.32	41.15	36.39	32.69	29.82	27.60	25.98	24.92	24.53	7.8
8.0	57.10	48.68	42.31	37.40	33.58	30.61	28.33	26.65	25.56	25.16	8.0
8.2	58.74	50.04	43.47	38.40	34.47	31.41	29.06	27.33	26.20	25.78	8.2
8.4	60.38	51.41	44.62	39.41	35.36	32.21	29.79	28.00	26.84	26.41	8.4
8.6	62.01	52.77	45.78	40.41	36.24	33.00	30.51	28.68	27.49	27.04	8.6
8.8	63.65	54.13	46.94	41.42	37.13	33.80	31.24	29.36	28.13	27.67	8.8
9.0	65.30	55.50	48.10	42.43	38.02	34.60	31.97	30.03	28.77	28.30	9.0
9.2	66.94	56.86	49.26	43.43	38.91	35.40	32.70	30.71	29.41	28.92	9.2
9.4	68.58	58.23	50.43	44.44	39.80	36.19	33.43	31.39	30.05	29.55	9.4
9.6	70.23	59.60	51.59	45.45	40.69	36.99	34.15	32.06	30.70	30.18	9.6
9.8	71.87	60.96	52.75	46.46	41.58	37.79	34.88	32.74	31.34	30.81	9.8
10.0	73.52	62.33	53.91	47.46	42.47	38.59	35.61	33.42	31.98	31.44	10.0
11.0	81.76	69.18	59.73	52.50	46.92	42.58	39.26	36.80	35.19	34.58	11.0
12.0	90.01	76.03	65.55	57.55	51.37	46.58	42.90	40.19	38.40	37.72	12.0
13.0	98.28	82.89	71.38	62.60	55.82	50.58	46.55	43.58	41.62	40.86	13.0
14.0	106.55	89.76	77.21	67.65	60.28	54.57	50.20	46.97	44.83	44.00	14.0
15.0	114.84	96.63	83.04	72.70	64.74	58.57	53.85	50.36	48.05	47.14	15.0
16.0	123.13	103.51	88.88	77.76	69.20	62.58	57.50	53.75	51.26	50.28	16.0
17.0	131.42	110.39	94.72	82.82	73.66	66.58	61.15	57.14	54.48	53.42	17.0
18.0	139.72	117.27	100.56	87.88	78.12	70.58	64.81	60.53	57.69	56.56	18.0
19.0	148.02	124.16	106.40	92.93	82.58	74.58	68.46	63.93	60.91	59.70	19.0
20.0	156.33	131.04	112.25	97.99	87.04	78.58	72.11	67.32	64.12	62.84	20.0
21.0	164.64	137.93	118.09	103.06	91.50	82.59	75.76	70.71	67.34	65.98	21.0
22.0	172.95	144.82	123.94	108.12	95.97	86.59	79.42	74.10	70.56	69.12	22.0
23.0	181.27	151.71	129.79	113.18	100.43	90.60	83.07	77.50	73.77	72.26	23.0
24.0	189.58	158.61	135.63	118.24	104.89	94.60	86.72	80.89	76.99	75.41	24.0
25.0	197.90	165.50	141.48	123.31	109.36	98.61	90.38	84.28	80.21	78.55	25.0
26.0	206.22	172.40	147.33	128.37	113.82	102.61	94.03	87.68	83.43	81.69	26.0
27.0	214.54	179.29	153.18	133.43	118.29	106.61	97.68	91.07	86.64	84.83	27.0
28.0	222.86	186.19	159.03	138.50	122.75	110.62	101.34	94.46	89.86	87.97	28.0
29.0	231.18	193.09	164.88	143.56	127.22	114.63	104.99	97.86	93.08	91.11	29.0
30.0	239.51	199.98	170.73	148.63	131.68	118.63	108.65	101.25	96.29	94.25	30.0

evaluated according to $\tau_0 = \mu\rho/\xi_0$. From (9), (15) and (18), we obtain IRPR

$$\sigma_0 R_H^{\theta}(\xi_0, \tau_0)/\eta = y_\mu \times 2 \times 3^{1/2}\pi(\tau_0)^2 \times h/A^* \qquad (23)$$

This can be calculated from the corresponding values of y_μ and A^*. Note that, for given $\mu\rho$, IRPR increases and y_μ decreases with increasing τ_0. The measured integrated reflecting power ratio, after multiplication by Q, is proportional to the value calculated with (23).

Table 3
Comparison of the calculated A^* values for different methods.

$\mu\rho$	θ_B	Calc. A	Calc. B	Dev. B × 0.1%	*IT*72	Dev. T × 0.1%
3	5	66.1663	66.23	+0.96	65.8	−5.57
	10	56.9361	56.95	+0.24	56.7	−4.16
	20	38.2720	38.29	+0.47	38.2	−1.89
	30	26.4343	26.45	+0.59	26.4	−1.30
	40	19.5042	19.51	+0.30	19.5	+0.02
	50	15.2748	15.28	+0.34	15.3	+1.65
	60	12.5860	12.59	+0.32	12.6	+1.11
	70	10.8644	10.87	+0.52	10.9	+3.28
20	5	5894.65	5913.70	+3.34	5790	−17.98
	10	2097.52	2103.10	+2.66	2100	+1.18
	20	648.117	650.11	+3.08	649	+1.36
	30	316.771	317.64	+2.74	317	+0.72
	40	191.303	191.76	+2.37	192	+3.64
	50	131.045	131.30	+1.95	131	−0.34
	60	97.9948	98.13	+1.38	98.4	+4.13
	70	78.5846	78.65	+0.83	78.7	+1.47

A: A^* calculated with the method of Thorkildsen & Larsen (1998*b*); the accuracy is better than 10^{-6}. B: A^* calculated with (15). Dev. B: the deviation of B from A. *IT*72: A^* from Vol. II of *International Tables for X-ray Crystallography* (1972). Dev. T: the deviation of *IT*72 from A.

6. Influence of the mosaic distribution upon IRPR and the extinction factor

6.1. Rocking curve

Figs. 7(*a*) and 7(*b*) show the angular dependence of P_H/P_0 for a cylindrical crystal with a Gaussian mosaic distribution for different ξ_0, $\tau_0 = 0.5$ and 2.5, and $\theta_B = 10^\circ$. The power ratio P_H/P_0 or $\mathrm{RPR}^{\mathrm{av}}$ as a function of $\Delta\theta_0/\eta$ for a cylindrical crystal defined by θ_B, τ_0 and ξ_0 is evaluated using

$$\sum_{n=1}^{n_{\max}} P_H[\xi(\Delta\theta_0/\eta), \tau(\Delta\theta_0/\eta), m_{\max}(n)]/(n_{\max}P_0^0).$$

The peak value $P_H/P_0 = 0.5114$ of the rocking curve for $\tau_0 = 2.5$, $\xi_0 = 0$ and $\Delta\theta_0/\eta = 0$ (Fig. 7*b*) is only slightly larger than 0.4999 obtained for the Laue case of a plane crystal with a corresponding mean reduced thickness of $A_K = 16\tau_0/3\pi$ and $\tau_0 = 2.5$. In addition, the peak value of the rocking curve $\tau_0 = 2.5$, $\xi_0 = 1$ and $\Delta\theta_0/\eta = 0$ in Fig. 7(*b*) may be obtained by dividing the total area under the $\tau_0 = 2.5$ curve of Fig. 3 by $2\tau_0 = 5$, *i.e.* $0.149/5 = 0.0298$.

Contrary to the P_H/P_0 curve for a crystal plate at given ξ_0 and Bragg geometry (Hu, 1997*a*), the areas under the P_H/P_0 *versus* $\Delta\theta_0/\eta$ curves may in some cases be greater for small τ_0 than for larger τ_0 if $\xi_0 > 0$ and $\theta_B \leq 70^\circ$. For example, the area under the $\tau_0 = 0.5$ curve in Fig. 7(*a*) is obviously greater than the one under the $\tau_0 = 2.5$ curve in Fig. 7(*b*) for $\xi_0 = 0.5$. However, the measured rocking curve of a cylindrical crystal is $(P_H/P_0) \times 2\tau_0$ and the area under this curve always increases with the size of the cylinder. For given τ_0 and ξ_0, the area under the rocking curve increases with θ_B.

6.2. IRPR and extinction factor for different mosaic distributions

Fig. 8(*a*) shows the $\sigma_0 R_H^\theta/\eta$ *versus* τ_0 curves for three different kinds of mosaic distribution: rectangular, Gaussian and Lorentzian for $\theta_B = 10^\circ$ and $\xi_0 = 0.5$, 1.0 and 2.0. For the same reduced radius τ_0, IRPR for the Gaussian and Lorentzian distributions is larger than for the rectangular distribution at small ξ_0, and almost the same for all distributions at $\xi_0 = 2.0$. The difference is due to the wings of the distributions. The power ratio of the rocking curve for a rectangular distribution is constant for $|\Delta\theta_0/\eta| \leq 3^{1/2}$. It is zero otherwise while, for the Gaussian and Lorentzian distributions, $\tau_0(\Delta\theta_0/\eta)$ continues to show appreciable values if τ_0 is large as shown in Fig. 7(*b*). At small ξ_0, this results in larger half widths of the rocking curves $(P_H/P_0) \times 2\tau_0$ for the latter distributions. Since the wing of the rocking curve of a Lorentzian distribution extends much further than that of a Gaussian distribution with the same ξ_0 and τ_0, IRPR for the Lorentzian distribution is remarkably larger than for the Gaussian ($\xi_0 \leq 0.5$). Sabine (1988) mentioned that the extinction factor for a non-absorbing cylindrical crystal with a Lorentzian distribution and for the Laue case is divergent when τ_0 is large. However, crystals with Lorentzian-like distributions do exist and thus the long tails may create problems. For example, the value of $[1 + (\pi/2) \times (\Delta\theta_0/\eta)^2]^{-1}$ for $\Delta\theta_0/\eta = 14$ is 0.00323 times the peak value at $\Delta\theta_0/\eta = 0$, and the total area under the tail from $\Delta\theta_0/\eta \geq 14$ is 3.3% of the total area of the distribution. For a crystal with $\xi_0 < 0.2$ and $\tau_0 > 5$, the area of the rocking curve for $\Delta\theta_0/\eta \geq 14$ may be several times larger than 3.3%. Since it is hard to imagine a crystal with such a long-tailed mosaic distribution and the above-mentioned effect exists only for

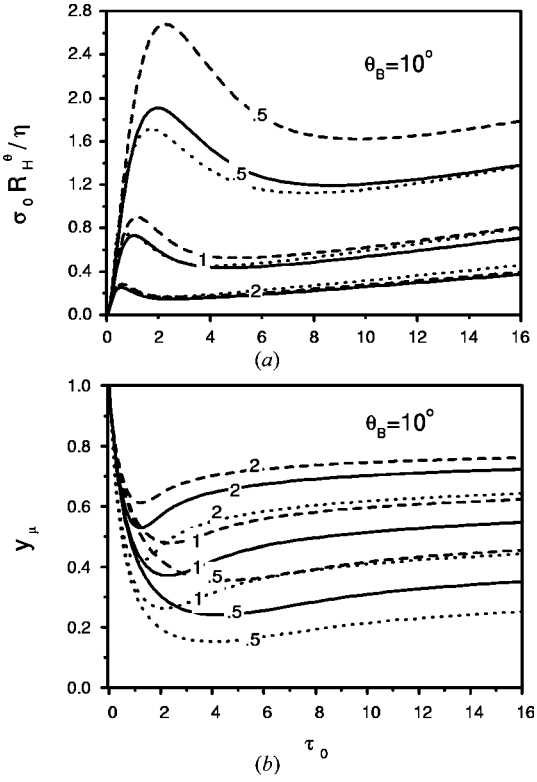

Figure 8
Comparison of three kinds of mosaic distributions for cylindrical crystals: (*a*) the dependence of $\sigma_0 R_H^\theta/\eta$ on τ_0; (*b*) the dependence of y_μ on τ_0. Rectangular distribution dotted line; Gaussian distribution solid line, Lorentzian distribution dashed line. The labels give ξ_0.

weak- or non-absorbing crystals and becomes negligible for crystals with $\xi_0 > 0.5$, an improved Lorentzian distribution $W'(\Delta\theta_0)$[6] is substituted for (6) in order to avoid the divergence of the extinction factor for large weak- or non-absorbing cylindrical crystals.

Fig. 8(*b*) shows y_μ evaluated with (3)–(18) using the same parameters as for Fig. 8(*a*). For given ξ_0 and τ_0, y_μ increases when going from a rectangular to a Gaussian and then to a Lorentzian distribution, but the difference between these distributions becomes smaller when $\xi_0 \geq 2$.

Hamilton (1957, 1963) has compared the extinction factors for a rectangular and a Gaussian distribution with the same η in non-absorbing cylindrical crystals for $\tau_0 \leq 1$, $\theta_B = 0$ and 90°. For the Gaussian, y_μ was 14% larger than for the rectangular distribution when $\theta_B = 0°$. In the present paper, the abscissa of Fig. 8(*b*) is τ_0. According to the definition of σ_0 in (10) and (13), τ_0 for a Gaussian distribution should be $2 \times 3^{1/2}/(2\pi)^{1/2} = 1.38\tau_0$ for a rectangular distribution at the same ρ and η. Thus, y_μ shown in Fig. 8(*b*) at $\tau_0 = 1$, $\theta_B = 10°$ and $\xi_0 = 0.5$ is 0.363 for a Gaussian and 0.309 for a rectangular distribution. The difference of 17% is in good agreement with Hamilton (1957).

7. Conclusions

The diffraction from a cylindrical crystal is due to a unique mixed geometry formed by a Bragg–Bragg reflection region with varying symmetry wedged into a Laue–Laue zone (Fig. 1). For large $\mu\rho$, the Bragg–Bragg region is responsible for the sharp peak in the intensity profile, the approximate $\sin^2\theta_B$ law of IRPR and the rapid change of y_μ at low θ_B. The results obtained here are not restricted to mosaic crystals but may also be helpful for diffraction and extinction studies in perfect and real cylindrical and spherical crystals.

For an absorbing cylindrical crystal at all θ_B, the intensity ratio distribution extends over all of $2\tau_0$ if $\mu\rho \leq 0.5$. In contrast, at $\mu\rho > 5$, *i.e.* $\tau_0 > 5/\xi_0$ where the geometry is essentially the Bragg case, the main part of the exit beam comes from the region before point **g** (Fig. 1), particularly when $\theta_B > 10°$ and $\xi_0 > 1$. This applies also to very small θ_B, but the central angle extended by **fg** is then very small and y_μ approaches the pure Bragg-case value only when $\mu\rho$ is extremely large.

The dip in the curve of the extinction factor y_μ against τ_0 and the large decrease of y_μ at small θ_B are important effects, since they may occur at $\mu\rho$ as low as 2.0 with corresponding values of $\tau_0 = 2.0/\xi_0$ and $\xi_0 > 0.2$, a rather common situation in the refinement of diffraction data. This large decrease of y_μ with decreasing θ_B at low angles indicates that severe extinction observed there in real cylindrical or spherical crystals is mainly caused by the incoherence of diffraction from different blocks, and it is then not necessary to introduce block-size-affected extinction. An example is the successful refinement of diffraction data of an LiF crystal plate, supposing exclusively secondary extinction at all θ_B (Hu, 1997*b*).

It is worth pointing out that the curves P_H/P_0 *versus* $\sigma_0 X/\xi_0$ for given θ_B and $\mu\rho$ have similar shapes for all ξ_0. Moreover, the curves IRPR *versus* $\tau_0\xi_0$, as well as y_μ *versus* $\tau_0\xi_0$, also depict the same property as shown in Fig. 8. Therefore, ξ_0 is an approximate scaling parameter. The limiting value of y_μ at $\theta_B = 90°$ and for large τ_0 is given by (22).

For given θ_B and $\mu\rho$, the magnitude of IRPR is determined by τ_0 or ξ_0. The average number of reflections the exit beam undergoes within the crystal decreases with increasing ξ_0 and as a result IRPR decreases and y_μ increases.

When $\xi_0 > 2$, the power ratio distribution and y_μ for given ξ_0 and τ_0 becomes progressively less sensitive to the kind of mosaic distribution, and increasingly so at larger θ_B owing to the larger angle subtended by **fg**, resulting in Bragg diffraction geometry. When $\xi_0 < 0.2$ and $\tau_0 > 10$, y_μ for the Lorentzian distribution is noticeably larger than for the Gaussian distribution.

Based on this work, detailed tables of y_μ as functions of θ_B, $\mu\rho$ and $\sigma_0 R$ will be presented in a subsequent paper for non-absorbing and absorbing spherical crystals with Gaussian and Lorentzian mosaic distributions.

APPENDIX *A*
Equation of a circle in oblique coordinates

Let $\mathbf{i}_x$, $\mathbf{i}_y$ be the unit vectors of Cartesian coordinates and $\mathbf{i}_N$, $\mathbf{i}_M$ be the unit vectors of oblique coordinates enclosing an angle $2\theta_B$. Let **P** be any vector with coordinates (x, y) referred to the Cartesian axes and (n, m) referred to the oblique axes.

$$\mathbf{P} = n\mathbf{i}_N + m\mathbf{i}_M \tag{24a}$$

$$= x\mathbf{i}_x + y\mathbf{i}_y. \tag{24b}$$

Let

$$i_N = i_x \tag{25a}$$

$$\mathbf{i}_M = \cos 2\theta_B \mathbf{i}_x + \sin 2\theta_B \mathbf{i}_y. \tag{25b}$$

The equation is also valid for $2\theta_B > 90°$. Substituting (25*a*) and (25*b*) into (24*a*), we get

$$\mathbf{P} = n\mathbf{i}_x + m(\cos 2\theta_B \mathbf{i}_x + \sin 2\theta_B \mathbf{i}_y). \tag{26}$$

Expressing x and y in terms of n and m gives

$$x = n + m\cos 2\theta_B \tag{27a}$$

$$y = m\sin 2\theta_B. \tag{27b}$$

The equation of the circle in the Cartesian coordinates with its center at $(\rho/\tan\theta_B, \rho)$ (see Fig. 1) is

$$(x - \rho/\tan\theta_B)^2 + (y - \rho)^2 = \rho^2. \tag{28}$$

Define $OC = e = \rho/\tan\theta_B$ (Fig. 1). From (27*a*) and (27*b*), the equation of the circle in the oblique coordinates is

$$(n + m\cos 2\theta_B - e)^2 + (m\sin 2\theta_B - \rho)^2 = \rho^2. \tag{29}$$

Collecting the coefficients of various powers of m, we get

[6] $W'(\Delta\theta_0)$ is used instead of $W(\Delta\theta_0)$ in (6) if $\xi_0 \leq 0.3$ and $\tau_0 > 5$. $W'(\Delta\theta_0)$ is defined as $W'(\Delta\theta_0) = 1.033W(\Delta\theta_0)$ if $|\Delta\theta_0| \leq 14\eta$; and 0 otherwise.

$$m^2 + 2m[(n-e)\cos 2\theta_B - \rho \sin 2\theta_B] + (n-e)^2 = 0. \quad (30)$$

The solutions of the quadric equation are

$$m = -(n-e)\cos 2\theta_B - \rho \sin 2\theta_B \mp \{\sin^2 2\theta_B[\rho^2 - (n-e)^2] - 2\sin 2\theta_B \cos 2\theta_B \rho(n-e)\}^{1/2}. \quad (31)$$

The $-$ and $+$ signs in (31) give the intersections of the circle and the straight line parallel to $\mathbf{i}_M$ with intercept n.

From (31), we get $m = \rho/\tan\theta_B$ for $n = 0$.

The author is grateful to Professor Z. Yang of the Neutron Scattering Laboratory of CIAE and Professor D. Schwarzenbach for valuable discussions, suggestions and help, and to Dr R. Fawcett and Professor R. Brugger for their help and valuable suggestions concerning the presentation.

References

Al Haddad, M. & Becker, P. J. (1990). *Acta Cryst.* A**46**, 112–123.
Authier, A. (2001). *Dynamical Theory of X-ray Diffraction. IUCr Monographs on Crystallography*. IUCr/Oxford University Press.
Bacon, G. E. & Lowde, R. D. (1948). *Acta Cryst.* **1**, 303–314.
Becker, P. (1975). *Acta Cryst.* A**31**, 417–425.
Becker, P. (1977). *Acta Cryst.* A**33**, 243–249.
Becker, P. & Coppens, P. (1974*a*). *Acta Cryst.* A**30**, 129–147.
Becker, P. & Coppens, P. (1974*b*). *Acta Cryst.* A**30**, 148–153.
Becker, P. & Dunstetter, F. (1984). *Acta Cryst.* A**40**, 241–251.
Chukhovskii, F. N., Hupe, A., Rossmanith, E. & Schmidt, H. (1998). *Acta Cryst.* A**54**, 191–198.
Darwin, C. G. (1922). *Philos. Mag.* **43**, 800–829.
Fankuchen, I. (1937). *Nature (London)*, **139**, 193–194.
Hamilton, W. C. (1957). *Acta Cryst.* **10**, 629–634.
Hamilton, W. C. (1963). *Acta Cryst.* **16**, 609–611.
Hu, H.-C. (1992). *J. Appl. Cryst.* **25**, 731–736.
Hu, H.-C. (1997*a*). *Acta Cryst.* A**53**, 484–492.
Hu, H.-C. (1997*b*). *Acta Cryst.* A**53**, 493–504.
Hu, H.-C. & Fang, Y. (1993). *J. Appl. Cryst.* **26**, 251–257.
Hu, H.-C., Shen, C-W., Li, Z-H., Qiao, Y. & Yang, B. (2001). *Chin. Phys. Lett.* **18**, 74–76.
International Tables for X-ray Crystallography (1972). Vol. II. Birmingham: Kynoch Press.
Kato, N. (1976*a*). *Acta Cryst.* A**32**, 453–457.
Kato, N. (1976*b*). *Acta Cryst.* A**32**, 458–466.
Kato, N. (1980*a*). *Acta Cryst.* A**36**, 171–177.
Kato, N. (1980*b*). *Acta Cryst.* A**36**, 763–769.
Kato, N. (1980*c*). *Acta Cryst.* A**36**, 770–778.
Kawamura, T. & Kato, N. (1983). *Acta Cryst.* A**39**, 305–310.
Lawrence, J. L. (1972). *Acta Cryst.* A**28**, 400–404.
Lawrence, J. L. (1973). *Acta Cryst.* A**29**, 208–210.
Maslen, E. N. (1995). *International Tables for Crystallography*, Vol. C, pp. 522–523. Dordrecht: Kluwer.
Olekhnovich, N. M. & Olekhnovich, A. I. (1980). *Acta Cryst.* A**36**, 22–27.
Sabine, T. M. (1988). *Acta Cryst.* A**44**, 368–373.
Sabine, T. M., Hunter, B. A., Sabine, W. R. & Ball, C. J. (1998). *J. Appl. Cryst.* **31**, 47–51.
Sears, V. F. (1989). *Neutron Optics.* Oxford University Press.
Sears, V. F. (1997). *Acta Cryst.* A**53**, 35–45.
Thorkildsen, G. & Larsen, H. B. (1998*a*). *Acta Cryst.* A**54**, 172–185.
Thorkildsen, G. & Larsen, H. B. (1998*b*). *Acta Cryst.* A**54**, 186–190.
Thorkildsen, G. & Larsen, H. B. (1999). *Acta Cryst.* A**55**, 1000–1013.
Werner, S. A., Arrott, A, King, J. S. & Kendrick, H. (1966). *J. Appl. Phys.* **37**, 2343–2350.
Werner, S. A. (1974). *J. Appl. Phys.* **45**, 3246–3254.
Wilkins, S. W. (1981). *Proc. Philos. Trans.* **299**, 275–317.
Zachariasen, W. H. (1967). *Acta Cryst.* **23**, 558–564.